Electronic Supplementary Information for Low-Cost Calculation and Analysis of 2D IR Spectra of Model Diiron Trinitrosyl Complexes in the NO Stretch Region with Vibrational Perturbation Theory

Hayden A. Moran,[1] Abigail F. Moody,[1] Mark A. Boyer,[1] Paul Garrett,[2] Manuel Quiroz,[1] Sarnali Sanfui,[1] Marcetta Y. Darensbourg,[1, a)] Carlos R. Baiz,[2, b)] and Daniel P. Tabor[1, c)]

[1)] *Department of Chemistry, Texas A&M University, College Station, TX*

[2)] *Department of Chemistry, The University of Texas at Austin, Austin, TX*

(Dated: 10 December 2025)

[a)]Electronic mail: marcetta@chem.tamu.edu

[b)]Electronic mail: cbaiz@cm.utexas.edu

[c)]Electronic mail: daniel_tabor@tamu.edu

CONTENTS

S1. DETAILS ON SYNTHETIC AND EXPERIMENTAL METHODS

A. Synthetic Methods

1. Materials and Methods

All reactions were performed in a N_2 atmosphere glovebox or by using the standard Schlenk line technique. All solvents were purified with an MBraun Manual Solvent Purification System with AcloaF200 activated alumina desiccant. All reagents were purchased from Sigma-Aldrich, TCI, and BTC, and used as received. The complexes, [1][BF_4], [2][BF_4], and *n*-pentyl nitrite, were synthesized according to published procedures.[S1–S3] The [^{15}NO][BF_4] reagent was prepared from a modified procedure, see below. NaBArF was purchased from Sigma-Aldrich. A Bruker Tensor Fourier Transform IR (FTIR) spectrometer was used to acquire infrared spectra with a CaF_2 cell.

2. Synthesis of [(NO)Fe(bme-dach)-Fe(NO)$_2$][BArF$_{24}$], [1][BArF$_{24}$]

In a 20 mL vial, 24 mg (0.027 mmol) of NaBArF and 12.6 mg (0.025 mmol) of [1][BF_4] were added, and then 5 mL of Et_2O was added to it. The reaction mixture was stirred overnight. The solid reactant gradually dissolved as the reaction approached completion. The solution was concentrated, and excess pentane was added to precipitate the product. The solid product was redissolved in Et_2O and filtered through Celite. Dark brown crystals of the product were grown by layering pentane into a solution of Et_2O at −35°C. Yield: 29 mg (∼90%). FTIR (CaF_2 windows, Et_2O, 23°C): ν(NO) = 1808, 1774, 1747 cm^{-1}.

3. Synthesis of [(NO)Fe(bme-dame)-Fe(NO)$_2$][BArF$_{24}$], [2][BArF$_{24}$]

In a 20 mL vial, 24 mg (0.027 mmol) of NaBArF and 12.5 mg (0.025 mmol) of [2][BF_4] were added, and then 5 mL of Et_2O was added to it. The reaction mixture was stirred overnight. The solid reactant gradually dissolved as the reaction approached completion. The solution was concentrated, and excess pentane was added to precipitate the product. The solid product was redissolved in Et_2O and filtered through Celite. Dark brown crystals of the product were grown by layering pentane into a solution of Et_2O at −35°C. Yield: 30 mg (∼90%). FTIR (CaF_2 windows,

Et_2O, 23°C): ν(NO) = 1809, 1780, 1743 cm^{-1}.

4. Synthesis of [^{15}NO][BF_4]

A 20 mL DCM solution containing 0.25 mL (1.86 mmol) of *n*–pentyl nitrite was cooled to −10°C, and 0.5 mL (1.86 mmol) of ∼55% w/w HBF_4·Et_2O was added dropwise. The reaction mixture was stirred for 30 min at −10°C. The white solid product was collected on a fritted glass Buchner filtering funnel and was washed with copious amounts of cold DCM. The product was transferred to a vial and dried under vacuum to yield 175 mg of product (80% yield).

5. X-ray crystallography

Single-crystal structure of [1][BArF] was measured at 110 K on a Bruker Quest X-ray (fixed-Chi geometry) diffractometer with a Mo-Iμs X-ray tube (K_α = 0.71073 Å). Single-crystal X-ray diffraction data for [2][BArF] were collected at 100 K on the BRUKER Venture X-ray (kappa geometry) diffractometer with Cu-Iμs X-ray tube (K_α = 1.5418 Å). Integrated intensity information for each reflection was obtained by reducing the data frames with the program APEX3.[S4] The data were then merged and scaled to generate a suitable dataset. Absorption effects were corrected using the program SADABS.[S5] Structure solutions were obtained readily with XT/XS in APEX3.[S6,S7] Hydrogen atoms were placed in idealized positions and refined in a riding model on their respective parent atoms. All non-hydrogen atoms were refined anisotropically. The absence of additional symmetry or significant voids was confirmed with PLATON (ADDSYM).[S8] Final refinement (weighted least squares on F^2) to convergence was carried out using Olex2.[S9]

B. 2D IR Spectral Collection Methods

2D IR spectroscopy measurements were performed using a custom-built spectrometer described previously.[S10] In brief, there are three pulses, centered at 5.8 μm: an excitation pulse pair (pump, ω_1) and a detection pulse (probe, ω_3). The axis present in the spectra are the x-axis (ω_1) and the y-axis (ω_3); the amplitude at a given data point corresponds to the signal emitted at a particular probe frequency ω_3 given a particular excitation frequency ω_1. The time between the final pump pulse and probe pulse was varied to observe vibrational transfer between nitrosyls. Each sample

TABLE S1. Crystal Data and Structure Refinement for [1][BArF] (CCDC 2322922)

Empirical formula	$C_{41}H_{30}BF_{24}Fe_2N_5O_3S_2$
Formula weight	1283.33
Temperature	110 K
Crystal system	Monoclinic
Space group	*P 1 21/c 1*
Unit cell dimensions	a = 14.3588(8) Å $\alpha = 90°$ b = 17.5509(9) Å $\beta = 100.940(2)°$ c = 19.2804(11) Å $\gamma = 90°$
Volume	4770.5(5) $Å^3$
Z	4
Radiation	Mo Kα (λ = 0.71073 Å)
Density (calculated)	1.787 g cm^{-3}
Absorption coefficient (μ)	0.836 mm^{-1} [a]
F(000)	2560
Crystal size	0.213 × 0.208 × 0.029 mm^3
Theta range for data collection	1.853 to 27.517°
Index ranges	$-18 \leq$ h ≤ 18, $-22 \leq$ k ≤ 22, $-25 \leq$ l ≤ 25
Reflections collected	10955
Independent reflections	9376 [R(int) = 1.029]
Completeness to theta = 25.242°	99.90%
Refinement method	Full-matrix least-squares on F^2
Data/restraints/parameters	9376 / 222 / 759
Goodness-of-fit on F^2 (GooF)	1.028
Final R indices [I > 2σ(I)]	R_1 = 0.0286, wR_2 = 0.0619
R indices (all data)	R_1 = 0.0377, wR_2 = 0.0670
Largest diff. peak and hole	0.521 and −0.381 e. $Å^{-3}$

[a] $R_1 = \sum(||F_o| - |F_c||)/\sum|F_o|$. [b] $wR_2 = [\sum[w(F_o^2 - F_c^2)^2]/\sum[w(F_o^2)^2]]^{1/2}$, $w = 1/[\sigma^2(F_o^2) + (ap)^2 + bp]$, where $p = [\max(F_o^2, 0) + 2F_c^2]/3$

TABLE S2. Crystal data and structure refinement for [2][BArF] (CCDC 2479069)

Empirical formula	$C_{40}H_{30}BF_{24}Fe_2N_5O_3S_2$
Formula weight	1271.32
Temperature	110 K
Crystal system	Triclinic
Space group	*P-1*
Unit cell dimensions	a = 12.8908(14) Å $\alpha = 90.780(4)^\circ$ b = 13.6374(15) Å $\beta = 93.632(5)^\circ$ c = 14.8069(16) Å $\gamma = 111.242(4)^\circ$
Volume	2419.4(5) $Å^3$
Z	2
Radiation	Cu Kα (λ = 1.54178 Å)
Density (calculated)	1.745 g cm^{-3}
Absorption coefficient (μ)	6.888 mm^{-1} [a]
F(000)	1268
Crystal size	0.195 × 0.151 × 0.064 mm^3
Theta range for data collection	2.993 to 70.475°
Index ranges	$-15 \leq$ h ≤ 15, $-16 \leq$ k ≤ 16, $-18 \leq$ l ≤ 18
Reflections collected	9228
Independent reflections	8583 [R(int) = 1.079]
Completeness to theta = 67.679°	100%
Refinement method	Full-matrix least-squares on F^2
Data/restraints/parameters	8583 / 568 / 805
Goodness-of-fit on F^2 (GooF)	1.053
Final R indices [I > 2σ(I)]	[a]R_1 = 0.0390, [b]wR_2 = 0.1046
R indices (all data)	[a]R_1 = 0.0420, [b]wR_2 = 0.1069
Largest diff. peak and hole	0.801 and −0.450 e. $Å^{-3}$

[a] $R_1 = \sum(||F_o| - |F_c||)/\sum|F_o|$. [b] $wR_2 = [\sum[w(F_o^2 - F_c^2)^2]/\sum[w(F_o^2)^2]]^{1/2}$, $w = 1/[\sigma^2(F_o^2) + (ap)^2 + bp]$, where $p = [\max(F_o^2, 0) + 2F_c^2]/3$

was measured at −20°C using a Specac cryostat (GS21525). The sample cell used was a liquid flow cell from Specac (GS20592) using a 25 μm spacer. N_2 gas purge was employed to minimise absorption from water in the air and liquid nitrogen as the coolant. All spectra were measured using a perpendicular pump–probe polarization condition to reduce scatter. Spectral acquisition time for 25 scan averages was approximately 3 minutes per spectrum. The 2D IR spectra were collected in THF.

S2. RESPONSE FUNCTION DERIVATION

The 2D IR spectra were calculated using third-order nonlinear response theory, which describes the molecular response to three sequential electromagnetic pulses. This approach requires evaluation of six response functions that correspond to different quantum mechanical pathways, represented by the Feynman diagrams shown in Figures S1 and S2. The three rephasing response functions are as follows:

$$R_1 = i\langle(\hat{\mu}_{0j}\cdot\hat{X})(\hat{\mu}_{0i}\cdot\hat{X})(\hat{\mu}_{0j}\cdot\hat{Z})(\hat{\mu}_{0i}\cdot\hat{Z})\rangle \exp(+i\omega_j t_1 - i(\omega_i-\omega_j)t_2 - i\omega_i t_3)\exp\left(-\frac{t_1+t_3}{T_{2,01}}-\frac{t_2}{T_{2,11}}\right) \quad (1)$$

$$R_2 = i\langle(\hat{\mu}_{0j}\cdot\hat{X})^2(\hat{\mu}_{0i}\cdot\hat{Z})^2\rangle \exp\left(+i\omega_j t_1 - i\omega_i t_3\right)\exp\left(-\frac{t_1+t_3}{T_{2,01}}\right) \quad (2)$$

$$R_3 = i\langle(\hat{\mu}_{0j}\cdot\hat{X})(\hat{\mu}_{0i}\cdot\hat{X})(\hat{\mu}_{ik}\cdot\hat{Z})(\hat{\mu}_{kj}\cdot\hat{Z})\rangle \exp\left(+i\omega_j t_1 - i(\omega_i-\omega_j)t_2 - i(\omega_k-\omega_j)t_3\right)\exp\left(-\frac{t_1}{T_{2,01}}-\frac{t_2}{T_{2,11}}-\frac{t_3}{T_{2,12}}\right), \quad (3)$$

where i and j index over the one quantum modes, k indexes over two quanta modes, t_1 and t_3 are scanned over for different waiting times between the pulses, t_2 is the constant population time, and $T_{2,\alpha\beta}$ are the dephasing times for the different interband and intraband coherences. Similarly, the non-rephasing response functions are as follows:

$$R_4 = i\langle(\hat{\mu}_{0j}\cdot\hat{X})(\hat{\mu}_{0i}\cdot\hat{X})(\hat{\mu}_{0i}\cdot\hat{Z})(\hat{\mu}_{0j}\cdot\hat{Z})\rangle \exp(-i\omega_j t_1 - i(\omega_j-\omega_i)t_2 - i\omega_j t_3)\exp\left(-\frac{t_1+t_3}{T_{2,01}}-\frac{t_2}{T_{2,11}}\right) \quad (4)$$

$$R_5 = i\langle(\hat{\mu}_{0j}\cdot\hat{X})^2(\hat{\mu}_{0i}\cdot\hat{Z})^2\rangle \exp\left(-i\omega_j t_1 - i\omega_i t_3\right)\exp\left(-\frac{t_1+t_3}{T_{2,01}}\right) \tag{5}$$

$$R_6 = i\langle(\hat{\mu}_{0j}\cdot\hat{X})(\hat{\mu}_{0i}\cdot\hat{X})(\hat{\mu}_{jk}\cdot\hat{Z})(\hat{\mu}_{ki}\cdot\hat{Z})\rangle$$
$$\exp\left(-i\omega_j t_1 + i(\omega_j-\omega_i)t_2 - i(\omega_k-\omega_i)t_3\right)\exp\left(-\frac{t_1}{T_{2,01}} - \frac{t_2}{T_{2,11}} - \frac{t_3}{T_{2,12}}\right). \tag{6}$$

The dipole terms of the response functions above are obtained using the following equation,

$$\langle(\hat{\alpha}\cdot\hat{E}_a)(\hat{\beta}\cdot\hat{E}_b)(\hat{\gamma}\cdot\hat{E}_c)(\hat{\delta}\cdot\hat{E}_d)\rangle =$$
$$\frac{1}{30}\{\cos\theta_{\alpha\beta}\cos\theta_{\gamma\delta}(4\cos\theta_{ab}\cos\theta_{cd} - \cos\theta_{ac}\cos\theta_{bd} - \cos\theta_{ad}\cos\theta_{bc})$$
$$+ \cos\theta_{\alpha\gamma}\cos\theta_{\beta\delta}(4\cos\theta_{ac}\cos\theta_{bd} - \cos\theta_{ab}\cos\theta_{cd} - \cos\theta_{ad}\cos\theta_{bc})$$
$$+ \cos\theta_{\alpha\delta}\cos\theta_{\beta\gamma}(4\cos\theta_{ad}\cos\theta_{bc} - \cos\theta_{ab}\cos\theta_{cd} - \cos\theta_{ac}\cos\theta_{bd})\}, \tag{7}$$

where $\hat{\alpha}$, $\hat{\beta}$, $\hat{\gamma}$, and $\hat{\delta}$ are arbitrarily oriented transition dipoles and the $\hat{E}_i$ terms are arbitrarily polarized pulses.

R_1, R_2, and R_3 are used to generate the rephasing diagrams, while R_4, R_5, and R_6 are used to generate the non-rephasing diagrams. After the summing of the rephasing and non-rephasing diagrams separately, a Fourier transform is applied to the rephasing and non-rephasing diagrams (eq 8 and eq 9), the ω_1 axis of the rephasing diagram sum is inverted, and the rephasing and non-rephasing diagrams are then summed. The real component of this sum is taken as the signal for the absorptive 2DIR spectrum. The spectra are normalized so that the maximum absolute value is 1.

$$R_{1,2,3}(t_3,t_2,t_1) = \sum_{n=1}^{3} R_n(t_3,t_2,t_1) \tag{8}$$

$$R_{4,5,6}(t_3,t_2,t_1) = \sum_{n=4}^{6} R_n(t_3,t_2,t_1) \tag{9}$$

$$S(\omega_3,t_2,\omega_1) = \int_0^\infty\int_0^\infty \sum_n iR_n(t_3,t_2,t_1)e^{i\omega_1 t_1}e^{i\omega_3 t_3}dt_1dt_3 \tag{10}$$

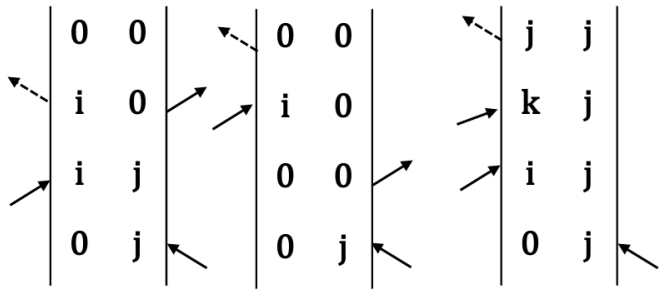

FIG. S1. Feynman diagrams used to generate rephasing diagrams and linear response functions R_1, R_2 and R_3 for arbitrary coupled oscillators i, j, and k.

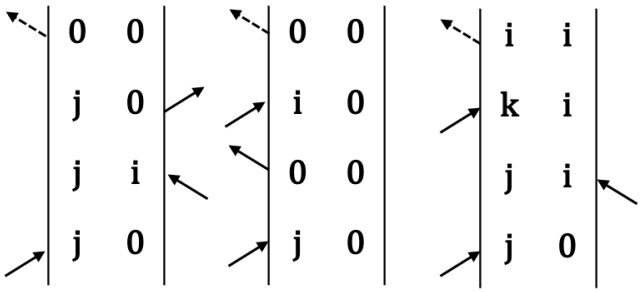

FIG. S2. Feynman diagrams used to generate non-rephasing diagrams and non-linear response functions R_4, R_5 and R_6 for arbitrary coupled oscillators i, j, and k.

S3. LOCALITY OF NO STRETCHES

To examine the locality of each fragment that forms the normal mode, we decomposed each normal mode into the 108 internal coordinates that form the system. This analysis quantifies how much each normal mode resembles a pure local vibration. In the matrices below, we report each matrix below with the three columns for each of the three normal modes. The rows represent the 3 N–O stretches, Fe–N–O bends, and Fe–N stretches, respectively, for each spin–redox state. In other words, the three columns are for each of the three normal modes, increasing frequency, rows 1–3 represent the N–O stretches, rows 4–6 represent the Fe–N–O bends, and the final three rows represent the Fe–N stretches. The ordering for the internal coordinates is consistent with the labeling scheme in Fig. 2Structural labels for internal coordinate and oblique coordinate decomposition.figure.caption.2.

TABLE S3. Normal Mode Internal Coordinate Decomposition for Cation

	BP86			TPSSh		
	Mode 1	Mode 2	Mode 3	Mode 1	Mode 2	Mode 3
NO_1	83.529439	0.303905	3.736132	82.824826	0.03445	6.040394
NO_2	0.59944	86.219937	1.151345	0.457404	85.951253	3.311276
NO_3	3.445489	1.383649	82.678024	5.345269	3.663904	80.262335
$FeNO_1$	0.056812	0.000782	0.004098	0.04096	0.000254	0.001394
$FeNO_2$	0	0.033914	0.005109	0.000049	0.016431	0.003508
$FeNO_3$	0.003461	0.000042	0.001376	0.003538	0.000238	0.003169
FeN_1	11.50767	0.036585	0.547848	10.237665	0.005665	0.604524
FeN_2	0.093494	11.401042	0.103606	0.054148	9.492045	0.327191
FeN_3	0.485601	0.226093	11.73756	0.830666	0.458943	9.383301

TABLE S4. Normal Mode Internal Coordinate Decomposition for Neutral

	BP86			TPSSh		
	Mode 1	Mode 2	Mode 3	Mode 1	Mode 2	Mode 3
NO_1	64.008397	16.779037	2.786382	80.171536	3.496161	0.765614
NO_2	19.732452	68.279139	1.170252	4.34283	82.571124	3.185187
NO_3	1.000052	2.936944	81.459442	0.077208	3.559387	84.073409
$FeNO_1$	0.049692	0.008281	0.002374	0.084003	0.001434	0.000002
$FeNO_2$	0.004185	0.028926	0.003419	0.000065	0.014827	0.003445
$FeNO_3$	0.010065	0.001418	0.009545	0.010133	0.000018	0.009814
FeN_1	12.403304	3.193447	0.5584	14.148056	0.713828	0.033885
FeN_2	2.253252	7.451665	0.115451	0.409154	8.249715	0.342439
FeN_3	0.189326	0.518696	13.783217	0.334497	0.565473	11.396375

The remaining percentage (not shown) is distributed over the other 99 internal coordinates in the full system.

All three of the normal modes are dominated by the N–O stretch. The BP86 method generally predicts more extensive coupling between the different N–O stretches than the TPSSh method, with the strongest mixing seen in the neutral complex.

TABLE S5. Normal Mode Internal Coordinate Decomposition for Anion

	BP86			TPSSh		
	Mode 1	Mode 2	Mode 3	Mode 1	Mode 2	Mode 3
NO_1	67.0811	9.05785	5.506613	84.319521	0.337813	1.989905
NO_2	12.119743	72.980078	1.505586	0.627873	86.953695	1.801349
NO_3	3.105843	3.881595	76.873456	1.220041	1.979569	84.253866
$FeNO_1$	0.04278	0.003382	0.00019	0.022474	0.000032	0.001105
$FeNO_2$	0.000803	0.008082	0.00089	0.000074	0.005054	0.000656
$FeNO_3$	0.01066	0.001936	0.020108	0.010021	0.000494	0.020974
FeN_1	14.888638	1.963244	1.162543	12.61697	0.061257	0.081241
FeN_2	1.823701	10.927571	0.215788	0.075424	10.056962	0.194222
FeN_3	0.645999	0.780746	14.484559	0.626321	0.321686	11.425151

The Fe–N stretches are the second largest contribution to most normal modes, ranging from 8–15%. These large contributions highlight the sensitivity of all observable properties of these modes to metal–ligand interactions, and thus, the importance of having an accurate electronic structure method for these interactions. However, the Fe–N–O bends contribute less than 0.1% to all three of these normal modes, thus, these modes are primarily stretches.

The neutral species exhibits the most delocalization, particularly when calculated with the BP86 method, while the cation maintains a high degree of locality at both levels of theory.

S4. UNSCALED IR SPECTRA

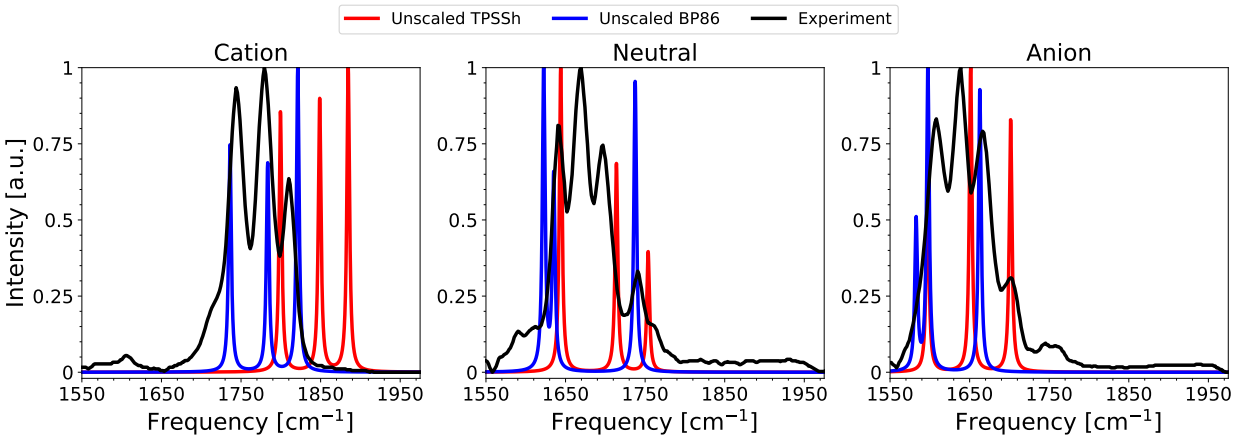

FIG. S3. FTIR spectra for the anionic, cationic and neutral species with the original unscaled traces with the both electronic structural treatments with experimental traces provided from Ghosh *et al.*[S2].

S5. UNSCALED 2D IR SPECTRA

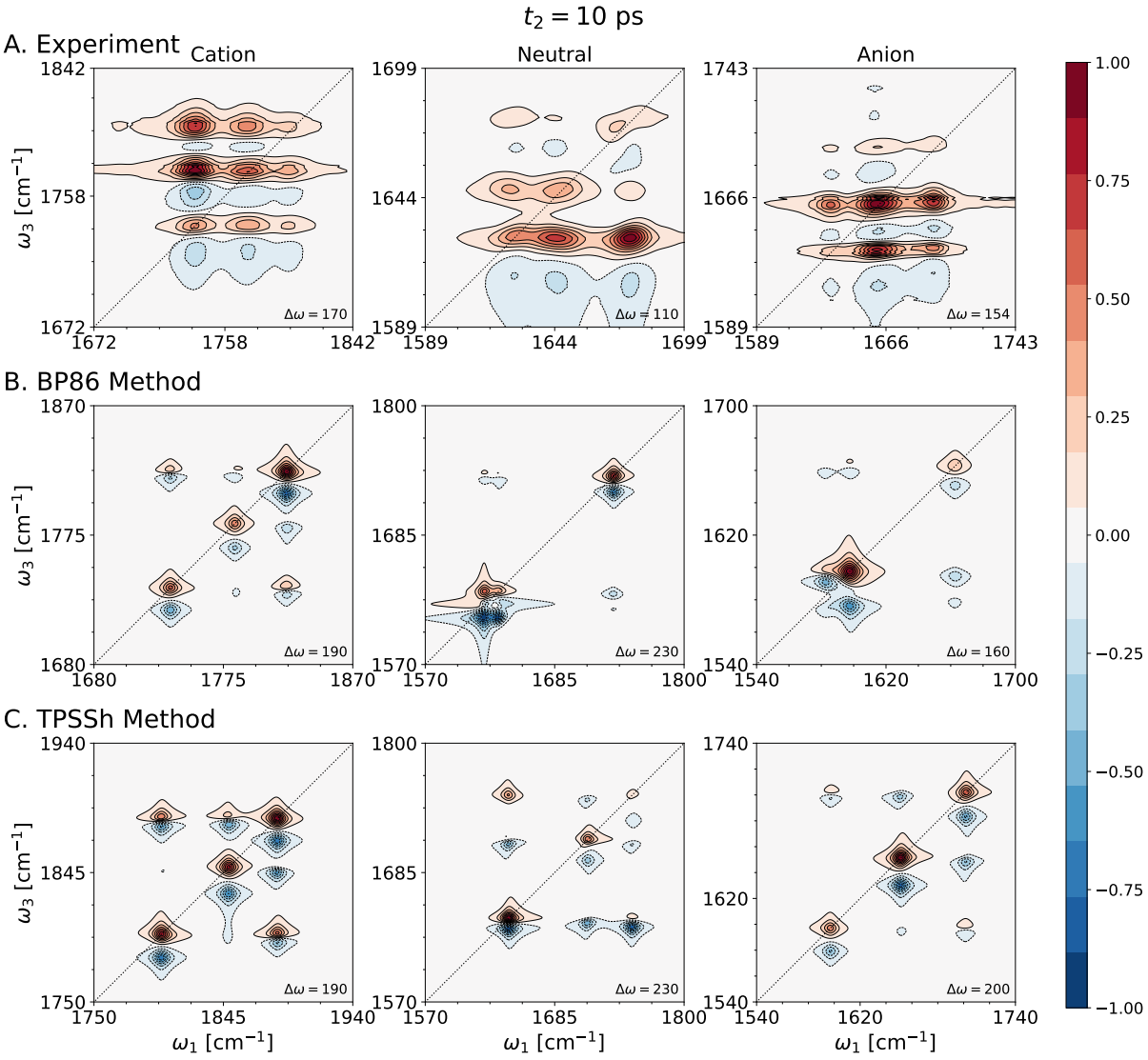

FIG. S4. A. Experimental 2DIR spectra, B. Theoretical 2DIR spectra at BP86/6-311++G(d,p) (C, H, O, N, S) and BP86/SDD (Fe), C. Theoretical 2DIR spectra at TPSSh/6-311++G(d,p)

S6. EFFECTIVE HARMONIC FREQUENCY SCALINGS

The scaling procedure consisted of the following steps. First, we calculated the anharmonic corrections for each vibrational mode using second-order vibrational perturbation theory. These anharmonic corrections were then rounded to the nearest whole wavenumber and added to the

TABLE S6. Experimental FTIR Frequencies (cm^{-1})

Mode Number	Anion	Cation	Neutral
1	1607	1743	1640
2	1637	1779	1668
3	1666	1809	1696

TABLE S7. Effective Harmonic Frequencies (cm^{-1})

Electronic Structure Treatment	Mode Number	Anion	Cation	Neutral
TPSSh	1	1624	1763	1671
	2	1662	1798	1689
	3	1685	1832	1745
BP86	1	1620	1761	1666
	2	1652	1800	1700
	3	1687	1833	1716

experimental FTIR frequencies, giving our estimate of the experimentally-derived harmonic frequencies (or effective harmonic frequencies).[S2] Finally, scaling factors were determined for each mode by finding the ratio of the computed harmonic frequency to these target frequencies.

This method effectively separates errors originating from harmonic frequency predictions and those associated with anharmonic coupling terms, since the first are effectively scaled out of the problem.

The experimental FTIR frequencies and derived effective harmonic frequencies are given in Tables S6 and S7, respectively.

TABLE S8. Mode-Specific Harmonic Frequency Scaling Factors

Electronic Structure Treatment	Mode Number	Anion	Cation	Neutral
TPSSh	1	1.006	0.969	0.997
	2	0.992	0.963	0.973
	3	0.979	0.960	0.968
BP86	1	1.015	1.004	1.011
	2	1.025	0.997	1.020
	3	1.002	0.994	0.977

S7. DIFFERENCES IN CROSS-PEAK SPLITTING UPON SCALING

TABLE S9. Cross-Peak Splitting Frequency Differences for Cation

Cation		BP86-Unscaled	BP86-Scaled	TPSSh-Unscaled	TPSSh-Scaled
Cross Peak	Transition	Frequency	Frequency	Frequency	Frequency
1	$\|000\rangle$ to $\|100\rangle$	1736.064	1742.963	1799.521	1742.614
	$\|010\rangle$ to $\|110\rangle$	1735.867	1742.684	1799.328	1742.368
		0.197	0.279	0.193	0.246
2	$\|000\rangle$ to $\|100\rangle$	1736.064	1742.963	1799.521	1742.614
	$\|001\rangle$ to $\|101\rangle$	1733.474	1740.29	1794.933	1737.603
		2.59	2.673	4.588	5.011
3	$\|000\rangle$ to $\|010\rangle$	1783.494	1778.744	1848.809	1778.248
	$\|100\rangle$ to $\|110\rangle$	1783.298	1778.465	1848.616	1778.002
		0.196	0.279	0.193	0.246
4	$\|000\rangle$ to $\|010\rangle$	1783.494	1778.744	1848.809	1778.248
	$\|001\rangle$ to $\|011\rangle$	1782.134	1777.346	1846.022	1775.204
		1.36	1.398	2.787	3.044
5	$\|000\rangle$ to $\|001\rangle$	1821.303	1808.62	1884.651	1808.764
	$\|100\rangle$ to $\|101\rangle$	1818.713	1805.947	1880.063	1803.753
		2.59	2.673	4.588	5.011
6	$\|000\rangle$ to $\|001\rangle$	1821.303	1808.62	1884.651	1808.764
	$\|010\rangle$ to $\|011\rangle$	1819.942	1807.222	1881.864	1805.72
		1.361	1.398	2.787	3.044

TABLE S10. Cross-Peak Splitting Frequency Differences for Neutral

Neutral		BP86-Unscaled	BP86-Scaled	TPSSh-Unscaled	TPSSh-Scaled
Cross Peak	Transition	Frequency	Frequency	Frequency	Frequency
1	$\|000\rangle$ to $\|100\rangle$	1622.546	1640.333	1643.921	1639.456
	$\|010\rangle$ to $\|110\rangle$	1611.124	1629.249	1641.676	1636.286
		11.422	11.084	2.245	3.17
2	$\|000\rangle$ to $\|100\rangle$	1622.546	1640.333	1643.921	1639.456
	$\|001\rangle$ to $\|101\rangle$	1621.916	1639.442	1637.224	1634.471
		0.63	0.891	6.697	4.985
3	$\|000\rangle$ to $\|010\rangle$	1635.103	1668.232	1713.938	1666.745
	$\|100\rangle$ to $\|110\rangle$	1623.681	1657.147	1711.694	1663.575
		11.422	11.085	2.244	3.17
4	$\|000\rangle$ to $\|010\rangle$	1635.103	1668.232	1713.938	1666.745
	$\|001\rangle$ to $\|011\rangle$	1633.807	1666.664	1711.188	1664.234
		1.296	1.568	2.75	2.511
5	$\|000\rangle$ to $\|001\rangle$	1737.496	1695.966	1753.787	1698.012
	$\|100\rangle$ to $\|101\rangle$	1736.866	1695.074	1747.09	1693.027
		0.63	0.892	6.697	4.985
6	$\|000\rangle$ to $\|001\rangle$	1737.496	1695.966	1753.787	1698.012
	$\|010\rangle$ to $\|011\rangle$	1736.2	1694.398	1751.037	1695.687
		1.296	1.568	2.75	2.325

TABLE S11. Cross-Peak Splitting Frequency Differences for Anion

Anion		BP86-Unscaled	BP86-Scaled	TPSSh-Unscaled	TPSSh-Scaled
Cross Peak	Transition	Frequency	Frequency	Frequency	Frequency
1	$\|000\rangle$ to $\|100\rangle$	1582.753	1607.844	1597.162	1607.261
	$\|010\rangle$ to $\|110\rangle$	1576.712	1602.117	1596.908	1606.911
		6.041	5.727	0.254	0.35
2	$\|000\rangle$ to $\|100\rangle$	1582.753	1607.844	1597.162	1607.261
	$\|001\rangle$ to $\|101\rangle$	1580.821	1605.866	1594.983	1604.917
		1.932	1.978	2.179	2.344
3	$\|000\rangle$ to $\|010\rangle$	1597.54	1637.406	1651.301	1637.271
	$\|100\rangle$ to $\|110\rangle$	1591.499	1631.678	1651.047	1636.921
		6.041	5.728	0.254	0.35
4	$\|000\rangle$ to $\|010\rangle$	1597.54	1637.406	1651.301	1637.271
	$\|001\rangle$ to $\|011\rangle$	1596.002	1635.747	1649.862	1635.625
		1.538	1.659	1.439	1.646
5	$\|000\rangle$ to $\|001\rangle$	1662.794	1666.179	1701.508	1665.554
	$\|100\rangle$ to $\|101\rangle$	1660.863	1664.201	1699.329	1663.21
		1.931	1.978	2.179	2.344
6	$\|000\rangle$ to $\|001\rangle$	1662.794	1666.179	1701.508	1665.554
	$\|010\rangle$ to $\|011\rangle$	1661.257	1664.521	1700.069	1663.908
		1.537	1.658	1.439	1.646

TABLE S12. Absolute Value of Differences in Cross Peak Splitting

Cross Peak	Transitions	BP86 Cation	TPSSh Cation	BP86 Neutral	TPSSh Neutral	BP86 Anion	TPSSh Anion
1	$\|000\rangle$ to $\|100\rangle$ $\|010\rangle$ to $\|110\rangle$	0.082	0.053	0.338	0.925	0.314	0.096
2	$\|000\rangle$ to $\|100\rangle$ $\|001\rangle$ to $\|101\rangle$	0.083	0.423	0.261	1.712	0.046	0.165
3	$\|000\rangle$ to $\|010\rangle$ $\|100\rangle$ to $\|110\rangle$	0.083	0.053	0.337	0.926	0.313	0.096
4	$\|000\rangle$ to $\|010\rangle$ $\|001\rangle$ to $\|011\rangle$	0.038	0.257	0.272	0.239	0.121	0.207
5	$\|000\rangle$ to $\|001\rangle$ $\|100\rangle$ to $\|101\rangle$	0.083	0.423	0.262	1.712	0.047	0.165
6	$\|000\rangle$ to $\|001\rangle$ $\|010\rangle$ to $\|011\rangle$	0.037	0.257	0.272	0.425	0.121	0.207

S8. MATHEMATICAL DERIVATION OF CROSS-PEAK SPLITTING AND ANALYSIS OF CUBIC FORCE CONSTANTS IN THREE-MODE SYSTEMS

The cross-peak splitting in a 2D IR spectrum results from anharmonic coupling between vibrational modes. For a three-mode system, the cross-peak splitting is given by the difference between the frequency of the transition from the state with one quantum in mode 2 to the combination state with one quantum in modes 1 and 2 and the frequency of the transition from the ground state to the state with one quantum in mode 1. That is,

$$\Delta E = (E_{110} - E_{010}) - (E_{100} - E_{000}) \tag{11}$$

In the framework of vibrational perturbation theory and the $\underline{\underline{X}}$-matrix formalism, the energy levels E_n are given by:

$$E_n = E_0 + \sum_i \omega_i \left(n_i + \frac{1}{2}\right) + \sum_{i>j} X_{ij} \left(n_i + \frac{1}{2}\right)\left(n_j + \frac{1}{2}\right), \tag{12}$$

where ω_i are the harmonic frequencies, n_i are the vibrational quantum numbers, and the elements X_{ij} are the anharmonic couplings.

This gives us an excited state transition frequency of

$$\begin{aligned} E(110) - E(010) = X_{11}\left(\left(1+\frac{1}{2}\right)^2 - \frac{1}{4}\right) + \frac{1}{2}X_{12}\left(\left(1+\frac{1}{2}\right)\left(1+\frac{1}{2}\right) - \left(1+\frac{1}{2}\right)\left(\frac{1}{2}\right)\right) \\ + \frac{1}{2}\sum_{i\neq 1,2} X_{1i}\left(\left(1+\frac{1}{2}\right)\left(\frac{1}{2}\right) - \frac{1}{4}\right) \end{aligned} \tag{13}$$

and the corresponding ground state transition frequency

$$\begin{aligned} E(100) - E(000) = X_{11}\left(\left(1+\frac{1}{2}\right)^2 - \frac{1}{4}\right) + \frac{1}{2}X_{12}\left(\left(1+\frac{1}{2}\right)\left(\frac{1}{2}\right) - \frac{1}{4}\right) \\ + \frac{1}{2}\sum_{i\neq 1,2} X_{1i}\left(\left(1+\frac{1}{2}\right)\left(\frac{1}{2}\right) - \frac{1}{4}\right) \end{aligned} \tag{14}$$

with a frequency splitting of

$$\begin{aligned} \Delta E =& \frac{1}{2}X_{12}\left(\left(1+\frac{1}{2}\right)\left(1+\frac{1}{2}\right) - \left(1+\frac{1}{2}\right)\left(\frac{1}{2}\right)\right) - X_{12}\left(\left(1+\frac{1}{2}\right)\left(\frac{1}{2}\right) - \frac{1}{4}\right) \\ =& \frac{1}{2}X_{12}\left(\left(1+\frac{1}{2}\right)^2 - \frac{1}{4}\right) \\ =& X_{12} \end{aligned} \tag{15}$$

When considering only the potential contributions, this is given by

$$\begin{aligned}\Delta E =& X_{12} \\ =& \frac{f_{1122}}{4} - \frac{1}{4}\sum_k \frac{f_{11k}f_{22k}}{\omega_k} \\ & - \frac{1}{8}\left(f_{112}^2\left(\frac{1}{2\omega_1+\omega_2}+\frac{1}{2\omega_1-\omega_2}\right)+f_{122}^2\left(\frac{1}{\omega_1+2\omega_2}+\frac{1}{-\omega_1+2\omega_2}\right)\right) \\ & - \frac{1}{8}\sum_{k\neq 1,2} f_{12k}^2\left(\frac{1}{\omega_1+\omega_2+\omega_k}+\frac{1}{\omega_1-\omega_2+\omega_k}+\frac{1}{-\omega_1+\omega_2+\omega_k}+\frac{1}{-\omega_1-\omega_2+\omega_k}\right)\end{aligned} \tag{16}$$

For clarity in the main text, we use commas to separate all indices of force constant subscripts.

For modes with similar frequencies, as encountered in the iron-nitrosyl systems studied here, the cubic force constant contributions often dominate the observed splitting patterns. This explains why the analysis in the main text focuses primarily on cubic derivatives when interpreting differences between electronic structure methods.

1. Alternate derivation in state-space path formalism

Without the introduction of the anharmonic X-matrix, this may also be evaluated in a state-space path formalism. We being by noting that at second order in perturbation theory,

$$E_n = \langle n|\, H^{(2)}|n\rangle + \sum_{m\neq n} \frac{\langle n|\, H^{(1)}|m\rangle\, \langle m|\, H^{(1)}|n\rangle}{E_n - E_m} \tag{17}$$

with our choice of $H^{(2)}$ containing the contributions from the quartic terms in the potential as well as kinetic contributions and $H^{(1)}$ containing the contributions from the cubic terms in the potential.

The contribution to ΔE from the quartic terms is straightforward, given by

$$\Delta E^{(2)} = (\langle 110|\, H^{(2)}|110\rangle - \langle 010|\, H^{(2)}|010\rangle) + (\langle 100|\, H^{(2)}|100\rangle - \langle 000|\, H^{(2)}|000\rangle) \tag{18}$$

to evaluate this, we consider each difference in turn, focusing for convenience only on the potential contribution

$$\begin{aligned}&\langle 110\,|V_{ijkl}q_iq_jq_kq_l|\,110\rangle - \langle 010|V_{ijkl}q_iq_jq_kq_l|010\rangle = \\ &\qquad V_{1111}\left(\langle 1|q_1^4|1\rangle - \langle 0|q_1^4|0\rangle\right) + V_{11jj}\,\langle n_j|q_j^2|n_j\rangle\left(\langle 1|q_1^2|1\rangle - \langle 0|q_1^2|0\rangle\right)\end{aligned} \tag{19}$$

$$\begin{aligned}&\langle 100|V_{ijkl}q_iq_jq_kq_l|100\rangle - \langle\, 000|V_{ijkl}q_iq_jq_kq_l|000\rangle = \\ &\qquad V_{1111}\left(\langle 1|{q_1}^4|1\rangle - \langle 0|{q_1}^4|0\rangle\right) + V_{11jj}\langle n_j|{q_j}^2|n_j\rangle\left(\langle 1|{q_1}^2|1\rangle - \langle 0|{q_1}^2|0\rangle\right)\end{aligned} \tag{20}$$

therefore the overall difference is given by

$$\langle 110|V^{(2)}|110\rangle - \langle 010|V^{(2)}|010\rangle - \Big(\langle 100|V^{(2)}|110\rangle - \langle 000|V^{(2)}|000\rangle\Big) = V_{1122}\left(\langle 1|{q_2}^2|1\rangle - \langle 0|{q_2}^2|0\rangle\right)\left(\langle 1|{q_1}^2|1\rangle - \langle 0|{q_1}^2|0\rangle\right) \quad (21)$$

and then as $V_{1122} = f_{1122}/4!$ but we have 6 permutations of these indices, we have

$$\Delta E^{(2)} \approx \frac{f_{1122}}{4} \quad (22)$$

The cubic contribution is more involved, but it is still possible to evaluate in the same manner. The generic cubic energy for state (i, j, k) is

$$\begin{aligned}\epsilon_{ijk} = & \frac{H(\pm 1,0,0)^2}{\pm\omega_1} P_{\pm 1}(n_i) \\ & + \frac{H(\pm 3,0,0)^2}{\pm 3\omega_1} P_{\pm 3}(n_i) \\ & + \frac{H(\pm 2,\pm 1,0)^2}{\pm 2\omega_1 \pm \omega_2} P_{\pm 2}(n_i) P_{\pm 1}(n_j) \\ & + \frac{H(\pm 1,\pm 1,\pm 1)^2}{\pm\omega_1 \pm \omega_2 \pm \omega_3} P_{\pm 1}(n_i) P_{\pm 1}(n_j) P_{\pm 1}(n_k) \\ & + \text{permutations}\end{aligned} \quad (23)$$

where $P_{\pm a}(n)$ is a polynomial contribution for that specific change in quanta which becomes zero when decreasing quanta below zero and $H(n, m, l)$ is the set of terms in $H^{(1)}$ that can cause the specified change in quanta. Therefore, we have a reduced number of terms to evaluate, which we consider as above. We will not evaluate all terms, but only enough to give a sketch for how Eq. 16 may be developed.

The set of terms we will consider are given by

$$\begin{aligned}(\epsilon_{110} - \epsilon_{010}) - (\epsilon_{100} - \epsilon_{000}) = & \left(\frac{H(\pm 2,\pm 1,0)^2}{\pm 2\omega_1 \pm \omega_2}\left(P_2(1)^2 - P_2(0)^2\right)\left(P_1(1)^2 - P_1(0)^2\right)\right) \\ & + \frac{H(\pm 1,\pm 1,\pm 1)^2}{\pm\omega_1 \pm \omega_2 \pm \omega_3} P_3(0)^2\left(P_2(1)^2 - P_2(0)^2\right)\left(P_1(1)^2 - P_1(0)^2\right)\end{aligned} \quad (24)$$

Here are the terms involving two quanta of change in one mode and one quantum in another, with the same potential terms across both portions of the state-space path which change quanta

$$\begin{aligned}& \frac{V_{112}^2}{2\omega_1 + \omega_2}\left(\langle 1|q^2|3\rangle^2 - \langle\ 0|q^2|2\rangle^2\right)\left(\langle 1|q|2\rangle^2 - \langle 0|q|1\rangle^2\right) \\ & \quad + \frac{V_{122}^2}{\omega_1 + 2\omega_2}\left(\langle 1|q^2|3\rangle^2 - \langle\ 0|q^2|2\rangle^2\right)\left(\langle 1|q|2\rangle^2 - \langle 0|q|1\rangle^2\right) = \frac{1}{2}\left(\frac{V_{112}^2}{2\omega_1 + \omega_2} + \frac{V_{122}^2}{\omega\ _1 + 2\omega_2}\right)\end{aligned} \quad (25)$$

$$\frac{V_{112}^2}{2\omega_1-\omega_2}\left(\langle 1|q^2|3\rangle^2-\langle\ 0|q^2|2\rangle^2\right)\langle 1|q|0\rangle$$
$$+\frac{V_{122}^2}{-\omega_1+2\omega_2}\left(\langle 1|q^2|3\rangle^2-\langle 0|q^2|2\rangle^2\right)\langle 1|q|0\rangle=\frac{1}{2}\left(\frac{V_{112}^2}{2\omega_1-\omega_2}+\frac{V_{122}^2}{-\omega_{\ 1}+2\omega_2}\right) \quad (26)$$

and here are the changes involving one quantum of change in three modes

$$\frac{V_{123}^2}{8}\left(\frac{1}{\omega_1+\omega_2+\omega_3}+\frac{1}{\omega_1-\omega_2+\omega_3}+\frac{1}{-\omega_1+\omega_2+\omega_3}+\frac{1}{-\omega_1-\omega_2+\omega_3}\right) \quad (27)$$

The total contribution is then the permutation-weighted sum of all of the terms.

S9. ADDITIONAL EXAMPLES OF CROSS-PEAK SPLITTING AND FREQUENCY DIFFERENCES

Complete tables of cross-peak frequency differences, transition moment vectors, and transition dipole magnitudes for all systems are provided in the supplementary data files (anion_splitting.csv, cation_splitting.csv, neutral_splitting.csv). These datasets contain the detailed anharmonic coupling parameters and transition properties underlying the cross-peak patterns observed in the 2D IR spectra. These datasets enable detailed comparison of cross-peak characteristics across different redox states.

S10. CURVILINEAR INTERNAL COORDINATE HESSIAN MATRICES

The complete 108×108 Hessian matrices can be retrieved in our GitHub repository. This section contains the 9×9 internal coordinate blocks of the Hessians, corresponding to the nine most important internal coordinates for the N–O stretch analysis: the three N–O stretches, the three Fe–N–O bends, and the three Fe–N stretches.

The matrix organization follows a similar pattern to Section S3, with rows/columns 1–3 corresponding to the N–O stretches, rows/columns 4–6 corresponding to the Fe–N–O bends, and rows/columns 7–9 corresponding to the three Fe–N stretches.

Elements of particular significance for understanding vibrational coupling are highlighted in bold throughout the matrices. These correspond to large off-diagonal coupling terms that indicate strong interactions between different vibrational coordinates.

The Hessian matrices below are presented for both electronic structure methods (TPSSh and BP86) across all three spin–redox states (cation, neutral, anion). All values are given in units of cm^{-1}.

$$\underline{\underline{f}}^{TPSSh}_{Cation} = \begin{pmatrix} 1766.24 & & & & & & & & \\ 10.45 & 1822.15 & & & & & & & \\ 42.76 & 14.03 & 1841.82 & & & & & & \\ 31.83 & 0.40 & 6.58 & 347.44 & & & & & \\ -5.71 & 64.31 & -8.49 & -0.26 & 279.22 & & & & \\ 1.04 & 3.62 & 21.36 & 147.41 & -7.26 & 323.11 & & & \\ \mathbf{9.34} & -3.27 & -20.39 & 56.32 & 4.88 & -55.63 & 725.63 & & \\ 0.47 & 30.77 & 1.75 & 0.79 & 77.24 & 4.00 & -6.35 & 728.28 & \\ -21.30 & -2.67 & \mathbf{16.34} & -58.36 & 1.52 & 35.41 & -69.00 & -9.60 & 729.60 \end{pmatrix}, \quad (28)$$

$$\underline{\underline{f}}^{TPSSh}_{Neutral} = \begin{pmatrix} 1615.95 & & & & & & & & \\ 20.57 & 1711.32 & & & & & & & \\ 48.07 & 17.94 & 1733.13 & & & & & & \\ -36.87 & 4.15 & 26.27 & 402.82 & & & & & \\ -9.73 & 102.47 & -5.65 & -2.84 & 357.57 & & & & \\ 13.81 & -7.16 & 26.68 & 217.03 & 7.87 & 389.78 & & & \\ \mathbf{92.31} & -5.44 & -32.35 & 56.73 & 2.23 & -54.48 & 859.11 & & \\ -2.83 & 76.30 & 1.28 & -5.06 & 92.87 & 4.35 & 15.50 & 752.35 & \\ 24.35 & -4.38 & \mathbf{22.23} & 2.30 & 7.18 & 29.23 & -130.96 & 21.60 & 758.87 \end{pmatrix}, \quad (29)$$

$$\underset{=Anion}{f}^{TPSSh} = \begin{pmatrix} 1546.13 & & & & & & & & \\ 13.00 & 1618.69 & & & & & & & \\ 50.76 & 12.80 & 1644.65 & & & & & & \\ -40.57 & 3.21 & 3.26 & 365.73 & & & & & \\ -5.54 & 22.80 & -3.16 & -4.15 & 184.56 & & & & \\ 1.69 & -1.55 & 40.12 & 205.16 & 0.72 & 362.46 & & & \\ \mathbf{1.25} & 2.69 & -28.74 & -7.10 & -1.44 & -63.76 & 683.37 & & \\ -0.09 & -20.91 & 0.20 & 0.93 & 31.14 & 0.08 & 1.71 & 601.39 & \\ -6.28 & 1.38 & \mathbf{-6.02} & -59.66 & 0.61 & 45.05 & -152.03 & -4.08 & 713.87 \end{pmatrix}, \quad (30)$$

$$\underset{=Cation}{f}^{BP86} = \begin{pmatrix} 1711.13 & & & & & & & & \\ 11.71 & 1760.03 & & & & & & & \\ 33.39 & 12.73 & 1789.18 & & & & & & \\ 36.51 & 5.21 & 10.57 & 367.59 & & & & & \\ -6.85 & 63.44 & -9.92 & -14.09 & 319.07 & & & & \\ 6.39 & 5.28 & 2.04 & 155.27 & -16.29 & 366.89 & & & \\ \mathbf{82.11} & -4.73 & 2.25 & 57.08 & 4.41 & -51.65 & 837.47 & & \\ 3.29 & 88.46 & 4.77 & 12.41 & 104.77 & 9.74 & -11.98 & 834.04 & \\ -4.27 & -1.70 & \mathbf{86.43} & -51.23 & 8.03 & 15.74 & 29.95 & -18.68 & 844.96 \end{pmatrix}, \quad (31)$$

$$\underset{=Neutral}{f}^{BP86} = \begin{pmatrix} 1578.69 & & & & & & & & \\ 18.30 & 1638.65 & & & & & & & \\ 37.08 & 16.40 & 1684.48 & & & & & & \\ -19.43 & 6.84 & 8.56 & 369.64 & & & & & \\ -9.24 & 99.39 & -7.80 & -8.31 & 359.14 & & & & \\ 8.47 & -5.95 & 27.26 & 226.75 & 1.52 & 370.66 & & & \\ \mathbf{71.01} & -2.74 & 5.09 & 35.48 & -3.15 & -58.08 & 880.84 & & \\ 2.31 & 90.39 & -0.95 & -0.49 & 119.83 & -2.96 & -0.04 & 782.43 & \\ 9.54 & -2.41 & \mathbf{78.02} & -55.83 & 1.76 & 33.07 & 50.03 & 0.73 & 879.52 \end{pmatrix}, \quad (32)$$

$$\underline{\underline{f}}^{BP86}_{Anion} = \begin{pmatrix} 1512.41 & & & & & & & & & \\ 15.44 & 1554.23 & & & & & & & & \\ 44.90 & 14.72 & 1597.97 & & & & & & & \\ -24.14 & 5.04 & 5.32 & 372.61 & & & & & & \\ -4.80 & 54.63 & -3.44 & -2.50 & 253.63 & & & & & \\ 5.33 & -3.09 & 41.93 & 248.57 & 2.26 & 374.21 & & & & \\ \mathbf{64.40} & 0.20 & 7.03 & 24.90 & -2.61 & -53.99 & 890.14 & & & \\ -2.27 & 49.65 & -2.07 & -1.31 & 64.43 & 0.33 & 1.09 & 754.87 & & \\ 10.62 & -1.29 & \mathbf{68.99} & -54.11 & -0.23 & 45.50 & 50.33 & -0.91 & 887.54 & \end{pmatrix}, \quad (33)$$

respectively.

S11. OBLIQUE COORDINATE HAMILTONIANS

The oblique coordinate Hamiltonians below result from applying the scaling transformation described in the main text to the curvilinear internal coordinate Hessians. The same convention is used for bold text as in Section S10.

$$\underline{\underline{H}}^{TPSSh}_{Cation} = \begin{pmatrix} 1680.30 & & & & & & & & & \\ 4.93 & 1730.63 & & & & & & & & \\ 22.62 & 7.10 & 1752.37 & & & & & & & \\ -24.73 & 1.82 & 8.94 & 314.97 & & & & & & \\ -4.06 & -19.26 & -4.34 & -1.43 & 244.39 & & & & & \\ 4.53 & 0.10 & -6.99 & 84.80 & -2.75 & 300.93 & & & & \\ \mathbf{-404.95} & -1.82 & -14.55 & -5.43 & 0.23 & -19.84 & 663.61 & & & \\ -1.44 & \mathbf{-401.13} & 0.39 & 1.69 & -9.31 & 1.08 & -4.54 & 658.70 & & \\ -10.48 & -1.42 & \mathbf{-425.59} & -20.13 & 2.09 & 8.74 & -55.07 & -4.33 & 667.54 & \end{pmatrix}, \quad (34)$$

$$\underline{\underline{H}}^{TPSSh}_{Neutral} = \begin{pmatrix} 1517.36 & & & & & & & & \\ 11.16 & 1619.04 & & & & & & & \\ 22.66 & 9.21 & 1646.56 & & & & & & \\ -33.75 & 4.08 & 10.94 & 352.33 & & & & & \\ -6.61 & -20.84 & -4.21 & -2.18 & 288.72 & & & & \\ 14.65 & -6.09 & -7.74 & 121.29 & 5.82 & 360.29 & & & \\ \mathbf{-375.33} & -5.11 & -13.50 & 15.00 & -1.55 & -14.18 & 767.29 & & \\ -4.91 & \mathbf{-333.75} & -3.04 & -2.71 & -36.11 & 0.79 & 6.75 & 674.20 & \\ 13.81 & -5.39 & \mathbf{-407.84} & 8.11 & 3.19 & -0.22 & -91.85 & 9.07 & 693.02 \end{pmatrix}, \tag{35}$$

$$\underline{\underline{H}}^{TPSSh}_{Anion} = \begin{pmatrix} 1470.63 & & & & & & & & \\ 5.83 & 1545.12 & & & & & & & \\ 26.75 & 5.59 & 1567.18 & & & & & & \\ -20.43 & 2.39 & 6.03 & 315.41 & & & & & \\ -3.18 & -9.12 & -1.73 & -2.74 & 166.80 & & & & \\ 7.31 & -1.08 & -14.84 & 117.61 & 1.56 & 333.21 & & & \\ \mathbf{-374.57} & -0.29 & -8.35 & -4.63 & -1.71 & -17.36 & 625.49 & & \\ -1.66 & \mathbf{-382.01} & -1.59 & 1.18 & -1.48 & -0.57 & -1.07 & 551.98 & \\ 0.19 & -0.96 & \mathbf{-394.45} & -23.38 & 1.18 & -1.32 & -94.80 & -4.30 & 654.67 \end{pmatrix}, \tag{36}$$

$$\underline{\underline{H}}^{BP86}_{Cation} = \begin{pmatrix} 1612.97 & & & & & & & & \\ 5.17 & 1659.07 & & & & & & & \\ 13.87 & 6.06 & 1686.04 & & & & & & \\ -32.46 & 2.51 & 11.04 & 332.16 & & & & & \\ -4.15 & -23.75 & -5.83 & -7.90 & 279.61 & & & & \\ 6.41 & 0.12 & -4.76 & 85.96 & -6.13 & 338.26 & & & \\ \mathbf{-376.99} & -2.63 & -15.41 & -21.19 & 0.27 & -19.29 & 747.10 & & \\ -0.51 & \mathbf{-385.40} & 2.59 & 6.59 & -4.43 & 2.54 & -7.59 & 740.53 & \\ -11.21 & -0.29 & \mathbf{-409.79} & -17.94 & 4.84 & 8.06 & -18.07 & -9.23 & 755.13 \end{pmatrix}, \tag{37}$$

$$\underline{\underline{H}}^{BP86}_{Neutral} = \begin{pmatrix} 1484.92 & & & & & & & & & \\ 9.25 & 1546.02 & & & & & & & & \\ 13.24 & 8.37 & 1586.15 & & & & & & & \\ -31.15 & 4.93 & 8.60 & 324.06 & & & & & & \\ -5.81 & -26.07 & -4.45 & -4.88 & 287.81 & & & & & \\ 8.46 & -4.73 & -13.43 & 128.02 & 3.39 & 335.09 & & & & \\ \mathbf{-383.05} & -2.71 & -15.05 & -2.93 & -2.95 & -22.60 & 784.63 & & & \\ -1.00 & \mathbf{-320.78} & -2.45 & 0.23 & -28.74 & -2.69 & -2.06 & 691.95 & & \\ -11.58 & -3.31 & \mathbf{-400.25} & -22.52 & 2.07 & -1.65 & -17.18 & -1.95 & 781.99 & \end{pmatrix}, \tag{38}$$

$$\underline{\underline{H}}^{BP86}_{Anion} = \begin{pmatrix} 1422.89 & & & & & & & & & \\ 7.42 & 1468.43 & & & & & & & & \\ 17.00 & 7.01 & 1505.81 & & & & & & & \\ -27.59 & 3.55 & 4.05 & 319.99 & & & & & & \\ -3.04 & -12.78 & -2.08 & -2.54 & 220.65 & & & & & \\ 6.52 & -2.64 & -18.98 & 142.41 & 2.43 & 332.61 & & & & \\ \mathbf{-379.04} & -1.89 & -12.78 & -1.20 & -2.93 & -20.93 & 795.13 & & & \\ -3.26 & \mathbf{-360.27} & -3.14 & 0.14 & -9.71 & -0.42 & -0.95 & 677.30 & & \\ -12.49 & -2.86 & \mathbf{-385.42} & -23.64 & 0.79 & -9.78 & -17.52 & -2.55 & 791.94 & \end{pmatrix}, \tag{39}$$

respectively.

S12. COMPARISON OF ELECTRONIC STRUCTURAL RESULT WITH EXPERIMENTAL GEOMETRIES

The challenges of modeling the electronic structure of these iron-nitrosyl complexes across different spin and redox states are clear at the geometric level. Table S12 compares the calculated geometric parameters with the experimental crystal structures from prior work.[S2]

The Fe–Fe distance, which varies significantly with spin and redox state changes, shows discrepancies of up to 0.12 Å between calculated and experimental values. This metal–metal separation is

TABLE S13. Geometric Parameters for Key Components of Molecular Geometry as Spin and Redox State Changes

	Anion			Neutral			Cation		
Parameter	BP86	TPSSh	XRD	BP86	TPSSh	XRD	BP86	TPSSh	XRD
Fe–Fe Distance	3.074	3.089	3.168	2.820	2.796	2.923	2.679	2.832	2.713
N–Fe–N Angle (Dinitrosyl)	115.196	118.220	114.062	115.427	116.864	114.779	113.122	116.201	114.589
Sulfur Distances	3.224	3.269	3.189	3.080	3.063	3.065	3.218	3.249	3.150
N Distance in N_2S_2 Plane	2.972	2.939	2.859	2.870	2.844	2.785	2.842	2.814	2.783
Mononitrosyl									
O–N–Fe Angle	163.536	170.357	171.387	148.494	149.320	149.947	162.072	161.561	171.057
O–N Bond Distance	1.213	1.204	1.176	1.193	1.179	1.177	1.170	1.158	1.162
N–Fe Bond Distance	1.669	1.729	1.720	1.681	1.681	1.709	1.652	1.676	1.666
Parallel Dinitrosyl NO									
O–N–Fe Bond Angle	171.305	174.831	171.895	169.350	172.313	171.825	160.964	164.677	164.879
O–N Bond Distance	1.218	1.212	1.208	1.205	1.197	1.188	1.180	1.169	1.165
N–Fe Bond Distance	1.635	1.652	1.657	1.643	1.635	1.667	1.664	1.688	1.678
Perpendicular Dinitrosyl NO									
O–N–Fe Bond Angle	166.559	168.026	164.077	171.661	172.163	165.629	178.714	175.465	175.489
O–N Bond Distance	1.202	1.193	1.214	1.185	1.175	1.194	1.165	1.155	1.165
N–Fe Bond Distance	1.637	1.651	1.653	1.642	1.639	1.673	1.654	1.689	1.668

particularly sensitive to electronic structure, as it reflects the balance between metal–metal bonding and ligand field effects. The O–N–Fe bond angle in the mononitrosyl unit represents another structurally important parameter[S2] that proves challenging to reproduce computationally. For the anionic species, the BP86 method deviates by approximately 8° from the experimental angle, while the neutral species shows excellent agreement within 1°. The cationic system presents the greatest difficulty, with both electronic structure methods predicting angles that differ by up to 10° from the crystal structure.

Additional systematic errors appear in the N_2S_2 plane geometry, where both computational methods consistently overestimate the distance between nitrogen atoms by up to ~ 0.1 Å. This tendency suggests limitations in the theoretical treatment of the sulfur-containing ligand environ-

ment that may propagate through to the vibrational property predictions.

The experimental geometries reveal important structure–property relationships. The systematic lengthening of the mononitrosyl Fe–N bond from cation to anion correlates with the computed decrease in Fe–N frequencies (740 → 691 → 677 cm^{-1}), following expected length–frequency inverse correlation. However, a significant discrepancy appears in the dinitrosyl region. While experimental structures show equivalent N–O bond lengths for both dinitrosyl ligands, both electronic structure methods predict substantial asymmetry, particularly with the TPSSh method. This suggests the calculated N–O stretch frequency splittings may be artificially large, representing a limitation of current density functional approaches for these systems. Though our individual mode scaling attempted to fix this, it may have shortcomings with nearly degenerate local mode frequencies.

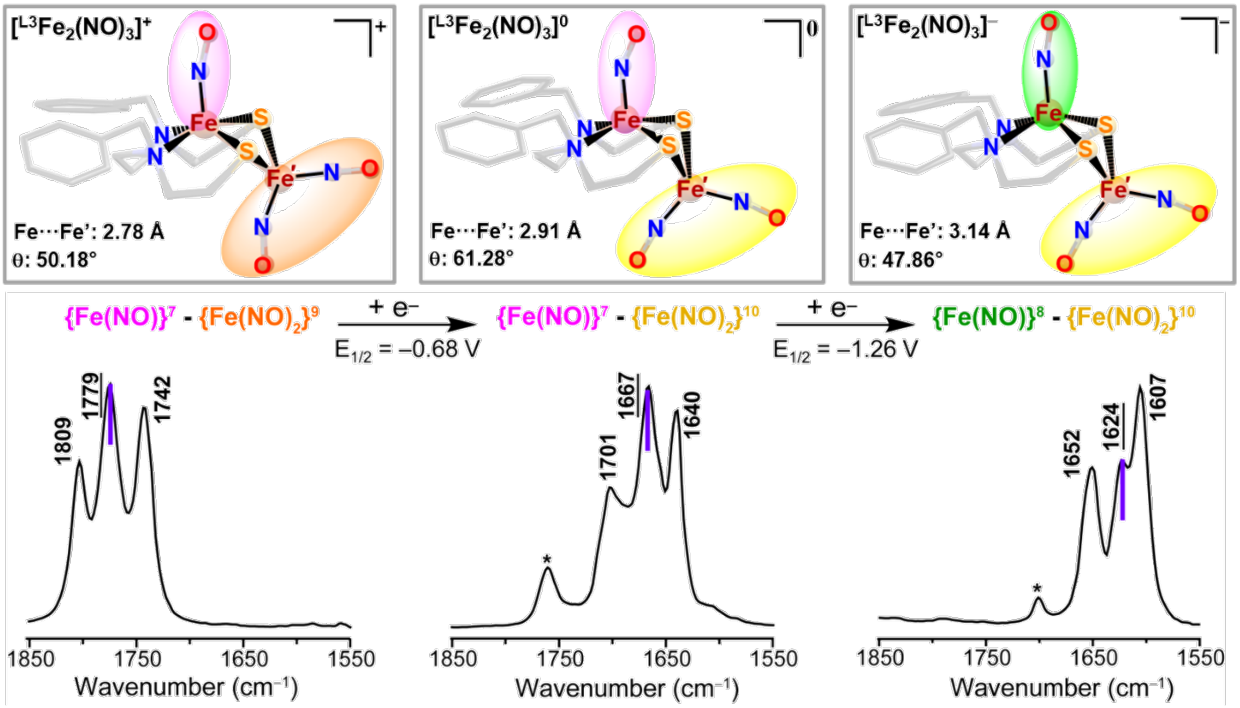

FIG. S5. Display of recently published SC-XRD-derived molecular structures of the $Fe_2(NO)_3$ complex in three charge levels; the color code for iron nitrosyls refers to the assigned primary positions of electron uptake: $Fe(NO)^7$ pink, $Fe(NO)^8$ green; $Fe(NO)_2{}^9$ orange; $Fe(NO)_2{}^{10}$ yellow). Below are the ν(NO) IR pattern and positions. An asterisk * on the IR spectra assigned to an undefined impurity as found in Sanfui *et al.*[S11]

S13. ELECTRONIC SUPPLEMENTARY INFORMATION

All electronic supplementary information can be found at the linked Zenodo repository: https://doi.org/10.5281/zenodo.17065451

REFERENCES

[S1]C.-H. Hsieh, S. Ding, Ö. F. Erdem, D. J. Crouthers, T. Liu, C. C. L. McCrory, W. Lubitz, C. V. Popescu, J. H. Reibenspies, M. B. Hall, and M. Y. Darensbourg, "Redox Active Iron Nitrosyl Units in Proton Reduction Electrocatalysis," Nature Communications **5**, 3684 (2014).

[S2]P. Ghosh, S. Ding, M. Quiroz, N. Bhuvanesh, C.-H. Hsieh, P. M. Palacios, B. S. Pierce, M. Y. Darensbourg, and M. B. Hall, "Structural and Electronic Responses to the Three Redox Levels of $Fe(NO)N_2S_2$-$Fe(NO)_2$," Chemistry – A European Journal **24**, 16003–16008 (2018).

[S3]N. G. Connelly, P. T. Draggett, M. Green, and T. A. Kuc, "Synthesis and reactivity of the tetrakis(acetonitrile)nitrosylrhodium dication," J. Chem. Soc., Dalton Trans. , 70–73 (1977).

[S4]"APEX3: Program for Data Collection on Area Detectors, BRUKER AXS Inc., 5465 East Cheryl Parkway, Madison, WI 53711–5373 USA,".

[S5]G. Sheldrick, "SADABS: Program for Absorption Correction of Area Detector Frames, BRUKER AXIS Inc., 5465 East Cheryl Parkway, Madison, WI 53711–5373 USA,".

[S6]G. M. Sheldrick, "*SHELXT* – Integrated space-group and crystal-structure determination," Acta Crystallographica Section A **71**, 3–8 (2015).

[S7]G. M. Sheldrick, "Crystal structure refinement with *SHELXL*," Acta Crystallographica Section C **71**, 3–8 (2015).

[S8]A. L. Spek, "Single-crystal structure validation with the program *PLATON*," Journal of Applied Crystallography **36**, 7–13 (2003).

[S9]O. V. Dolomanov, L. J. Bourhis, R. J. Gildea, J. A. K. Howard, and H. Puschmann, "*OLEX2*: a complete structure solution, refinement and analysis program," Journal of Applied Crystallography **42**, 339–341 (2009).

[S10]S. C. Edington, A. Gonzalez, T. R. Middendorf, D. B. Halling, R. W. Aldrich, and C. R. Baiz, "Coordination to Lanthanide Ions Distorts Binding Site Conformation in Calmodulin," Proceedings of the National Academy of Sciences **115**, E3126–E3134 (2018), https://www.pnas.org/doi/pdf/10.1073/pnas.1722042115.

[S11]S. Sanfui, M. Quiroz, J. Li, Y. Ha, F. Yang, J. Guo, N. Bhuvanesh, B. S. Pierce, P. B. Balbuena, P. A. Lindahl, M. B. Hall, and M. Y. Darensbourg, "Structural and Electronic Complexities of a Sulfur-Bridged Di-Iron Complex Composed of Mono- and Di-Nitrosyl Units," Advanced Science , e13976 (2025).